Antenna-enhanced high-resistance photovoltaic infrared detectors based on quantum ratchet architecture: Supplementary Material

Hideki T. Miyazaki,[a] Takaaki Mano, Takeshi Noda, Takeshi Kasaya, and Yusuf B. Habibullah[b]
Affiliations
National Institute for Materials Science, Tsukuba 305-0047, Japan
[a]**Author to whom correspondence should be addressed:** miyazaki.hideki@nims.go.jp
[b]**Present address:** Rakuten Mobile, Inc., Tokyo 158-0094, Japan.

S1. Current noise spectral density for the background state

The current noise spectral density for the background state $i_{\mathrm{nsd,BG}}$ is complicated compared with that for the dark state; therefore, the derivation of Eq. (4a) in the main text is presented here. The $i_{\mathrm{nsd,BG}}$ value is the shot noise by the detected background radiation from a 300 K environment [1,2]:

$$i_{nsd,BG} = \sqrt{\frac{2e}{N_w}\int R_{esp}(\lambda)P_{BG}(\lambda)Ad\lambda}, \qquad \text{(S1)}$$

where e is the electron charge, N_{w} the number of periods of the unit structure, R_{esp} the responsivity, P_{BG} the background Planck radiation intensity, A the detector area, and λ the wavelength. As shown in Eq. (2) in the main text, R_{esp} is proportional to the absorption efficiency η_{abs} and the escape probability p_{e}. In Eq. (S1), as the noise gain, $1/N_{\mathrm{w}}$ is considered. While some authors include p_{e} in the noise gain [1], our experimental results support the absence of p_{e} [2-4].

In the photovoltaic quantum-well infrared photodetectors (PV-QWIPs) discussed in this paper, the integration in Eq. (S1) can be simply described with values at the peak responsivity wavelength λ_{p} because the bandwidth is narrow:

$$\int R_{esp}(\lambda)P_{BG}(\lambda)d\lambda = R_{esp,p}P_{BG,p}\Delta\lambda, \qquad \text{(S2)}$$

where $R_{\mathrm{esp,p}}$ is the peak responsivity, $P_{\mathrm{BG,p}}$ the background Planck radiation intensity at λ_{p}, and $\Delta\lambda$ the effective bandwidth determined so that Eq. (S2) holds. Moreover,

$$R_{esp,p} = \frac{e\lambda_p}{hc} \times \frac{\eta_{abs,p}p_e}{N_w}, \qquad \text{(S3)}$$

where h is the Planck constant, c the speed of light, and $\eta_{\mathrm{abs,p}}$ the absorption efficiency at λ_{p}.

In reality, the background state is continuously connected with the dark state. Delga showed that i_{nsd}^2 is generally expressed as the sum of the shot noise and the Johnson noise [2]. This permits a discussion on the dependence of i_{nsd} on both the temperature of the detector T and the bias voltage V_{b}. In considering the Johnson noise, there can be two types of resistance R_0: a static one, $R_{\mathrm{s}} = dV/dI$ at $V_{\mathrm{b}} = 0$ (V: voltage, I: current), and a dynamic one, $R_{\mathrm{d}} = dV/dI$. Delga pointed out that those resistances should be properly selected depending on the polarity of V_{b}. According to our experimental results, however, neither exhibited a remarkable difference, although in practice R_{s} agreed well with the experiment throughout the entire V_{b} range.

While T is relatively high, Johnson noise is dominant; thus, the detector performance is described by the dark-state properties. However, as T decreases, both noises become comparable with each other [background-limited infrared photodetector (BLIP) temperature, T_{BLIP}]. At a sufficiently low T, the shot noise by the background radiation becomes dominant (BLIP region). Even in the T range of the BLIP region, the dark current drastically increases for elevated V_{b}, and the performance is described by the dark-state properties in the high V_{b} region. The BLIP operation holds within a finite V_{b} range near zero bias at a T range below T_{BLIP} (more details given in supplementary material S5).

S2. Calculation of the global transition rate and device resistance

In this work, global transition rates G_{ij} between the states i (S_i) and j (S_j) at equilibrium were calculated based on Koeniguer *et al.* [5] and Ferreira and Bastard [6]. G_{ij} gives the resistance-area product R_0A by Eq. (5) in the main text.

In this study, we applied several approximations in determining G_{ij}. In the calculation of transition rates S_{ij} based on Ferreira and Bastard [6], depending on the relative magnitude of the energetic distance ΔE and longitudinal optical (LO) phonon energy $\hbar\omega_{\mathrm{LO}}$, the initial or final state was fixed at their minimum energy point by ignoring the finite distribution of electron momentum. It was confirmed that the influence of this approximation is not essential. At $\Delta E \sim \hbar\omega_{\mathrm{LO}}$, S_{ij} exhibits singular behavior due to the resonant LO phonon scattering. To avoid unrealistic results, the damping coefficient of LO phonons of 0.25 meV was incorporated [7].

In the calculation of R_0A based on Koeniguer *et al.* [5], all possible intersubband paths have to be accounted for. In our work, the device layer is sandwiched by 48-nm-thick heavily doped contact layers. These relatively thin contact layers also work as quantum wells, and discrete subbands are formed in the contact layers as well. We conducted the calculation of the resistance R_0A considering all possible combinations of these states. However, it was found that R_0A at around 77 K, mainly discussed in this work, is well described by the simple summation between S_1 and S_j in the devices as shown in Eq. (5) in the main text. This means that the ground state S_1 works as a bottleneck, and this is a general feature in a wide temperature range. The R_0A obtained by Eq. (5) offers fairly good agreement with the experimental results, as presented in the inset of Fig. 5(a) in the main text.

However, at a relatively high temperature ($T > 140$ K), careful consideration of the electron transport between the contact layer and the states in the device becomes important. In a low temperature range ($T < 140$ K), among the transports between the left contact layer and S_j in the device region, the transport to S_1 is dominant. In contrast, in a high temperature range (T > 140 K), other direct paths from the left contact layer to individual states S_j in the device layer other than S_1 gradually become remarkable; i.e., currents irrelevant to the photoexcitation become outstanding. This leads to a discrepancy of R_0A between the calculation and experiment [inset of Fig. 5(a)] in a high temperature range. In addition, this reasonably explains the sudden decrease in responsivity in a high temperature range beyond 140 K, which is discussed in supplementary material S5. However, in this work, further details are not discussed.

Figure 1 quantitatively displays the significance of the spatial and energetic distances between S_1 and S_j on R_0A for a virtual, representative model case. As a typical wavefunction, we assume the ground state of a 5-nm-wide GaAs quantum well (QW) between AlGaAs barriers with a conduction band offset of $\Delta E_c = 0.3$ eV. The color indicates the G_{1j} between the ground state S_1 at the origin and a state with the identical wavefunction shape virtually placed at (Δz, ΔE) at 77 K. For generality, we assume that the energy level of S_1 is located at the Fermi level.

Here, we would like to make three remarks for interpreting Fig. 1. First, overall, G_{ij} values are underestimated by a few orders of magnitude compared with the actual values, since the energy level of S_1 is set to the Fermi level. Usually, S_1 is set below the Fermi level to fill S_1 with sufficient electrons. The actual electron densities of the other states are similarly higher, and they should exhibit greater conductance than the estimation in Fig. 1. Second, the G_{1j} values at the positions of $j = 8$ and 7, shown by color in Fig. 1, are overestimated by 1–2 orders of magnitude. This is because the actual wavefunctions for S_8 and S_7 have a very different form than the assumed shape, and their actual overlap with the wavefunction of S_1 should be much smaller. Finally, the G_{1j} values for the extraction region ($j \geq 5$) are underestimated. In reality, the wavefunctions other than that of S_1, particularly $j \geq 5$, extend over a wide space covering multiple QWs. Therefore, the overlap of the wavefunctions remains high for a large Δz, and it should give higher G_{1j} values than in Fig. 1.

The actual values of G_{1j} based on the band diagrams in Fig. 2 are shown by solid lines in Fig. S1. For reference, the values based on the model calculation at the gravity center positions plotted in Fig. 1 are also shown by dotted lines. From a comparison between the dotted and solid lines, we can confirm the above three features: The dotted lines are a few orders of magnitude lower as a whole, S_8 and S_7 are outstandingly high, and the reducing trend of the dotted lines associated with the state progress (from S_8 to S_1) is sharper. The most important point understood from the actual G_{1j} values (solid lines) is that S_6 and S_5 exhibit similar conductance as S_7 for the quantum cascade detector (QCD). To be precise, $G_{17} = 2.16 \times 10^{16}$ m^{-2}s^{-1}, G_{16}

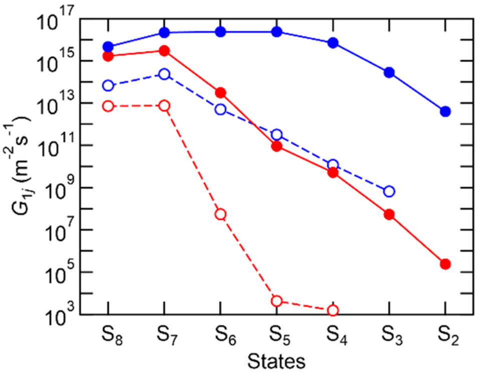

FIG. S1. Actual value of G_{1j} of each state S_j based on the band diagrams in Fig. 2 in the main text for QRD (red) and QCD (blue): solid lines and closed circles. Values of G_{1j} at the actual (Δz, ΔE) positions denoted by color in Fig. 1 in the main text are also shown by dotted lines and open circles.

$= 2.36 \times 10^{16}$ m^{-2}s^{-1}, and $G_{15} = 2.39 \times 10^{16}$ m^{-2}s^{-1}; all three of these are nearly equivalent, and S_5 gives the highest value. This is why the R_0A of the QCD was mainly determined by S_5 and S_6. In contrast, for the quantum ratchet detector (QRD), G_{16} is three orders of magnitude smaller that of the QCD, and G_{15} is smaller by more than five orders of magnitude, reflecting the exponential decay of the form factor against the spatial distance. Therefore, in the R_0A of the QRD, the contribution after S_6 is negligible, and R_0A is simply determined by S_8 and S_7. In the solid lines at S_8 and S_7 in Fig. S1, other important information can also be found. First, QRD shows lower values than QCD. This is because a large part of the wavefunction of the QRD flows out to the step QW W_2, and this leads to a smaller overlap with S_1. Next, S_7 is higher than S_8 for both detectors, since S_7 is energetically closer to S_1.

The estimation in Fig. 1 includes various inaccuracies as discussed above. Nevertheless, the diagram in Fig. 1 suggests some fundamental strategies as a semi-quantitative guideline expressing the overall trend. We believe the concepts presented in Fig. 1 offer a clear vision for the rational design of QW structures.

S3. Calculation of the conduction band diagram, wavefunction, and transition time

The conduction band profiles and the wavefunctions were numerically obtained by self-consistently solving the Schrödinger and Poisson equations (nextnano GmbH, nextnano3/++). Material parameters were based on Vurgaftman *et al.* [8]. However, a small correction was applied so that the calculation would give consistent results with the numbers of experiments; we used the conduction band offset ΔE_c between GaAs and Al$_x$Ga$_{1-x}$As as an adjustment parameter. Vurgaftman's original relationship $\Delta E_c = 0.66\ \Delta E_g$ (ΔE_g: bandgap difference) was slightly modified to $\Delta E_c = 0.61\ \Delta E_g$.

In the actual crystal growth by molecular beam epitaxy (MBE), errors in the thickness and composition arose. On the basis of X-ray diffraction and responsivity spectrum evaluated by a Brewster-angle detector, errors of +7% and -7% in the thickness and composition x, respectively, were assumed for the diagrams in Fig. 2.

The LO phonon scattering time τ_{ij} from S_i to S_j was calculated as $\tau_{ij} = n_i / G_{ij}$, where n_i is the two-dimensional electron density in S_i, based on the G_{ij} obtained according to supplementary material S2. For obtaining the total transition time through parallel paths S_8 and S_7, the oscillator strengths from S_1 to the respective states were taken into account.

The tunneling time from W_1 to W_2 was evaluated as half the duration of a Rabi oscillation cycle [9]. Nevertheless, the important dynamics was determined by the LO phonon scattering, since the tunneling (0.19–0.39 ps) is sufficiently faster than the LO phonon scattering in this study.

As shown in Eq. (3b) in the main text, the specific detectivity for the dark state D^*_{DK} of a PV-QWIP is determined by η_{abs}, p_e, R_0A, and N_w. In this study, η_{abs} was enhanced by optical antennas, and N_w was minimized ($N_w = 1$). Other parameters, p_e and R_0A are related to the overlap of the wavefunctions.

As shown in Eq. (5) in the main text, R_0A is given by G_{18}, G_{17},,, G_{12}. On the other hand, p_e is determined by the relative magnitudes between the transition rate from the excited states S_7 and S_8 in the forward direction (Γ_{for}) and that in the backward direction (Γ_{back}):

$$\Gamma_{\mathrm{for}} = 1/\tau_{76} + 1/\tau_{86} + 1/\tau_{\mathrm{for,others}},$$

and

$$\Gamma_{\mathrm{back}} = 1/\tau_{71} + 1/\tau_{81} + 1/\tau_{\mathrm{back,others}},$$

where $1/\tau_{\mathrm{for,others}}$ is a minor transition rate from S_7 and S_8 in the right direction except for S_6, and $1/\tau_{\mathrm{back,others}}$ is that in the left direction.

For maximizing R_0A, minimization of G_{16} by suppressing the overlap of the wavefunctions of S_6 and S_1 is of particular importance. On the other hand, for maximizing p_e, minimization of τ_{76} and τ_{86} by increasing the overlap of the wavefunctions of S_7/S_8 and S_6 is necessary. These requirements conflict with each other. In the present study, Γ_{for} for QRD (8.7×10^{11} s^{-1}) was smaller than that for QCD (1.22×10^{12} s^{-1}). This is because in the QRD, the wavefunction of S_6 overlaps only with the outer edges of those of S_7 and S_8.

However, quantitatively, there was no great difference between the estimated p_e values: 0.69 for QRD and 0.72 for QCD, only 4% difference. Therefore, we expect that QRDs can support both high R_0A and high p_e. We attribute this study's moderate p_e value for QRD to inappropriate material parameters, particularly the conduction band offset, in the QW design. We also observed a change in the optical/electronic properties due to wafer bonding. Further refinement of the QW design and fabrication process is necessary. However, in the previous studies on QCDs, correction of band alignment by biasing has been used as well [10,11]. Although the development of precisely designed quantum cascade lasers has been intensively promoted, further studies are still required for QW engineering based on very precise band alignment.

S4. Details on the fabrication, electromagnetic calculation, and characterization

Refer to the earlier work [12] for basic descriptions of the fabrication, electromagnetic calculation, and characterization. Only the details unique to the present paper are described in the following text.

The intrinsic properties of the QW structures grown using MBE were examined by fabricating test devices for dark current measurement and Brewster-angle detectors for responsivity, and then the results were fed back to the QW structure design. A few wafers judged to be promising were selected for wafer transfer and patch antenna fabrication.

Electromagnetic properties in this paper were obtained by finite element analysis (COMSOL, COMSOL Multiphysics). The semiconductor layer was divided into five regions: left contact, the first barrier, the first active QW, other device layers (called cascade layer), and the right contact layer. The dielectric constant of the cascade layer was obtained from the volume average of GaAs and AlGaAs. In the vertical component of the dielectric function of the first QW, a Lorentzian term $-\Omega_p^2/(\omega^2-\Omega^2+i\Gamma\omega)$ was applied. For our quantum ratchet detector (QRD) and the reference quantum cascade detector (QCD), we set $(\Omega, \Gamma, \Omega_p) = (189, 10.5, 130)$ and $(181, 13.0, 140)$ in meV, respectively, so that the maximum responsivity of the biased Brewster-angle detector (assumed as unity escape probability) and the calculated absorption would be consistent. The oscillator strengths f and the dipole matrix elements $<z>$ estimated from these values were $f = 0.65$ and $<z> = 1.39$ nm for QRD and $f = 0.71$ and $<z> = 1.48$ nm for QCD.

For the measurement of responsivity and noise, a Gifford-McMahon cryostat (NIKI Glass, LTS-101DL-IR-OPT-LV) was used. The current noise spectrum density i_{nsd} was obtained from a plateau region, as a peak in the histogram. The position of the plateau region typically falls within the frequency range of 10–1000 Hz. The plateau feature for the dark state was sensitive to the temperature; the position would be determined by the relationship of the impedance of the device and the current amplifier. For the dark state, the value to be measured (~10^{-15} A/Hz$^{1/2}$) was close to the limit of the amplifier.

S5. Other properties

This section presents important results that could not be shown in the main text. Figure S2 exhibits the measured absorption spectrum of the QRD (red curve), obtained from the microscopic reflection by the Fourier transform infrared spectrometer. Based on the choice of optimum size of the antenna arrays, nearly perfect absorption of 0.96 was obtained. Calculated absorption by each layer is also displayed. The total absorption is well reproduced by the calculation. As discussed for Fig. 4(b) in the main text, the absorption by the QW layer is about 0.2 at most. Other absorption takes place in the Au and contact layers, and then simply dissipates as heat rather than generating an optical signal. It has been suggested that the absorption in the QW layer η_{abs} could be improved with the proper choice of N_{w} [13]. Consequently, future improvement is expected. The results for the reference QCD are very similar, so they are not presented.

As shown in Figs. 4(b) and (c), R_{esp} spectra for QRD and QCD exhibit drastic changes by V_{b}. Here, we address the change in λ_{p}. Figures S3(a) and (b) show R_{esp} spectra at representative V_{b} values for QRD and QCD, respectively. The change in λ_{p} is summarized in Fig. S3(c). The stepwise shift is due to the resolution of the Fourier transform infrared spectrometer (16 cm^{-1}). λ_{p} generally showed a red shift up to 2 meV depending on the increase in V_{b}. However, an interesting behavior was found for the QCD. Within the general trend of the red shift, we observed a blue shift of 3 meV at an intermediate range of V_{b} = 0.12–0.20 V. This is due to the switching of the dominant excited states from S_7 to S_8. In Fig. S3(b), a widening of the spectrum due to the coexistence of two states was observed in the transition range (V_{b} = 0.16 and 0.20 V). In Fig.

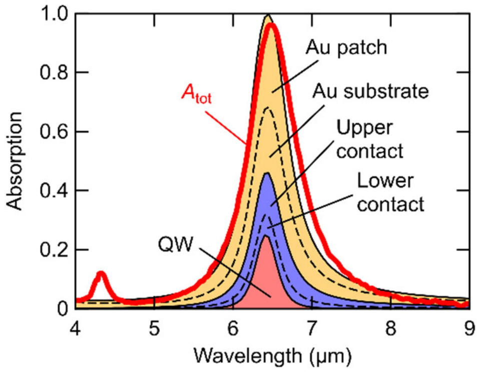

FIG. S2. Experimental absorption spectrum of antenna-enhanced QRD (red solid line). Calculated absorption ratio of each layer is also shown.

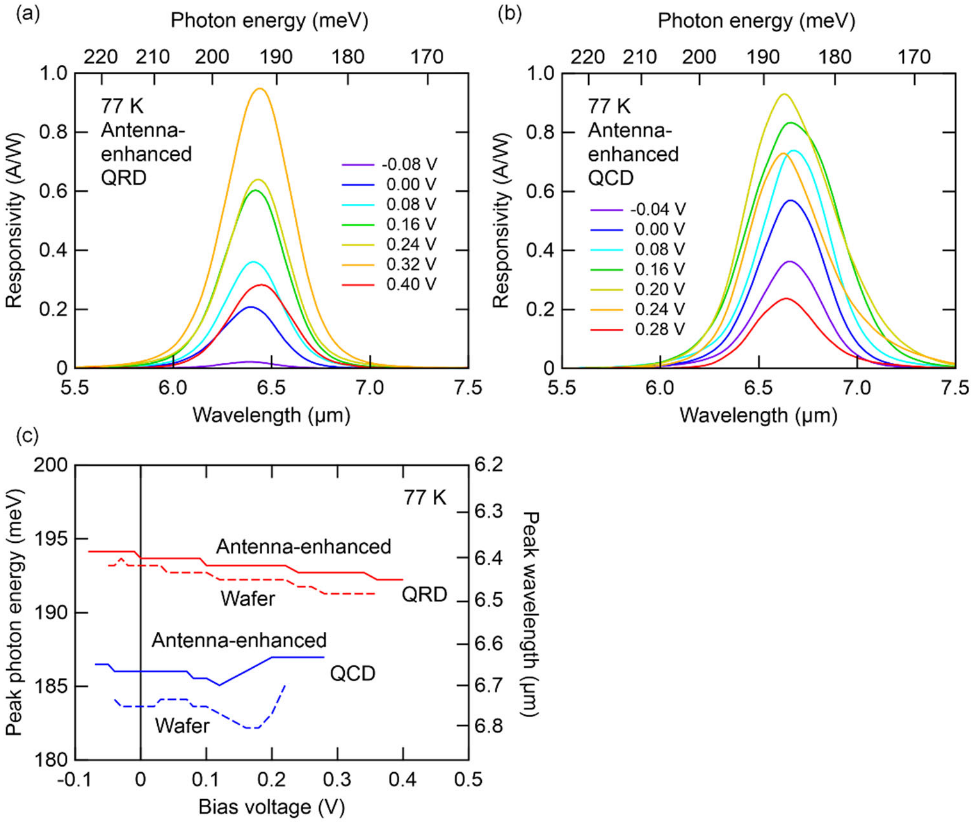

FIG. S3. R_{esp} spectra for (a) QRD and (b) QCD at representative V_b values. (c) V_b dependence of λ_p obtained from these spectra (solid lines) for QRD (red) and QCD (blue). Dotted lines show λ_p for wafers without antennas.

S3(c), the λ_p change in the wafers themselves without antennas, evaluated by Brewster-angle detectors, is also shown by dotted lines. It was confirmed that the blue-shift feature of the QCD originates from the QW structures (wafers). In an antenna-enhanced device, part of the R_{esp} spectrum of the wafer is enhanced by the resonance of the antennas.

Figure S4(a) shows the temperature dependence of the photovoltaic responsivity at zero bias. At low temperatures, the responsivity is nearly flat. However, at around 140 K, there is a sudden drop for both detectors. Although many QCDs have demonstrated room-temperature responsivity, in this work, the QCD also exhibited similar responsivity drop in the high temperature range. Therefore, the unfavorable high-temperature properties in this work would be due to a common reason for both detectors, rather than due to the QW design in the QRD. While QRD offers inferior zero-bias responsivity to QCD at 77 K, it exhibits greater response at $T > 160$ K. This suggests that QRD has greater potential for high-temperature operation than QCD.

As displayed in Fig. 4 in the main text, when biased, both the QRD and the QCD represent similar responsivity values. This is also denoted in Fig. S4(a) by the marks at 77 K. Conduction band diagrams of this high V_b situation are shown in Fig. S5. The excited states of the active well W_1 are confined at the tip of the barrier, and their right side is open. This is nearly the same situation as the conventional bound-to-bound photoconductive QWIPs. The photoelectrons escape from W_1 by tunneling. The tunneling times are estimated as 0.14 ps and 0.34 ps for QRD and QCD, respectively [3]. On the other hand, the backward transition times ($1/\Gamma_{\mathrm{back}}$) are 2.58 ps (QCD) and 2.12 ps (QCD) for zero bias. In our thin active wells (~ 5 nm), the influence of the electric field on the backward transition times would be small. From these values, we can estimate the escape probability

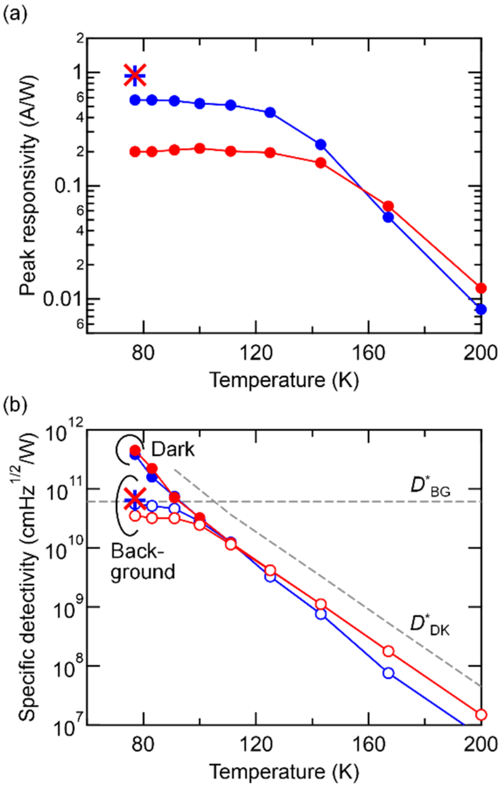

FIG. S4. (a) Temperature dependence of peak responsivity $R_{esp,p}$ at zero bias for QRD (red) and QCD (blue). Maximum $R_{esp,p}$ values at 77 K are shown by marks; cross: QRD, plus: QCD. (b) Temperature dependence of specific detectivity D^* at zero bias for QRD (red) and QCD (blue). Filled circles: dark state; open circles: background state. Maximum D^*_{BG} values at 77 K are denoted by marks; cross: QRD, plus: QCD. Gray dotted lines indicate predicted D^*_{DK} and D^*_{BG} for the QRD under the assumption of solving the band alignment issue.

as p_e = 0.95 (QRD) and 0.86 (QCD); thus, $p_e \sim 1$. By using this result, p_e for zero bias can be evaluated.

In conventional QWIPs at high V_b, R_{esp} generally saturates at a constant value [3]. Nevertheless, in Fig. 4(c), R_{esp} quickly decreased after showing these peaks. We attribute this sudden decrease to the same mechanism as the R_{esp} drop at $T > 140$ K. As can be expected from Fig. S5, at these high V_b values, direct transport from the left contact layer to individual states S_j, other than S_1, would become remarkable. Since currents irrelevant to the photoexcitation are outstanding, R_{esp} could suddenly decrease.

Figure S4(b) shows the temperature dependence of the D^* at zero bias. As for the D^*_{DK}, QRD is consistently superior to QCD, demonstrating the effect of high resistance. Despite the inferior zero-bias D^*_{BG} of QRD to QCD at 77 K, as seen in Fig. 5(b) in the main text, QRD demonstrates a higher performance at a finite bias voltage [denoted by marks in Fig. S4(b)].

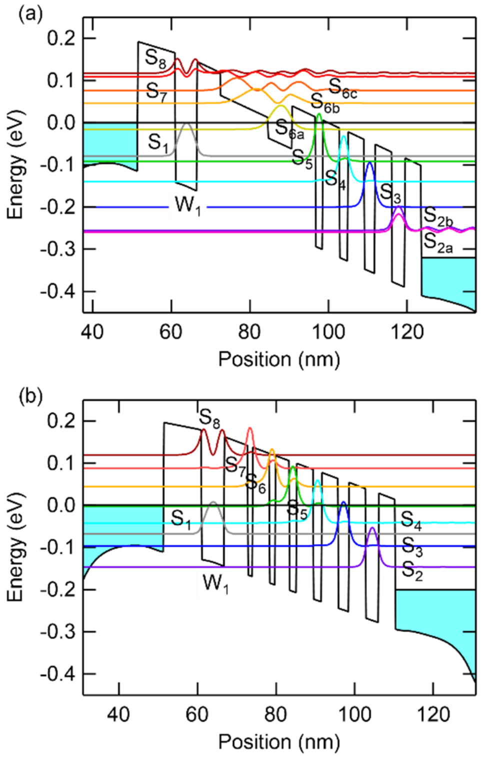

FIG. S5. Conduction band diagrams with squared wavefunction profiles for (a) QRD at V_b = 0.32 V and (b) QCD at V_b = 0.20 V.

Here, we would like to discuss the predicted performance of the QRD under the assumption of solving the band alignment issue. As shown in the calculation results (circles) in Fig. 4(b), η_{abs} values for the QRD and the QCD are equivalent. Improvement of p_e by a factor of ~3 is expected. In that case, Eqs. (3b) and (4b) predict the enhancement of D^*_{DK} by 3 times and D^*_{BG} by $\sqrt{3}$ times. These estimated properties are added to Fig. S4(b) using gray dotted lines. A zero-bias D^*_{BG} similar to that of the QCD would be possible. The most striking improvement would appear in T_{BLIP}, i.e., the movement of the crossing point of D^*_{DK} and D^*_{BG} as a result of the increase in D^*_{DK}. The present T_{BLIP} of 98 K could be increased to ~110 K, which would contribute to relaxing the required cooling power.

Figures S6(a) and (b) show the V_b dependence

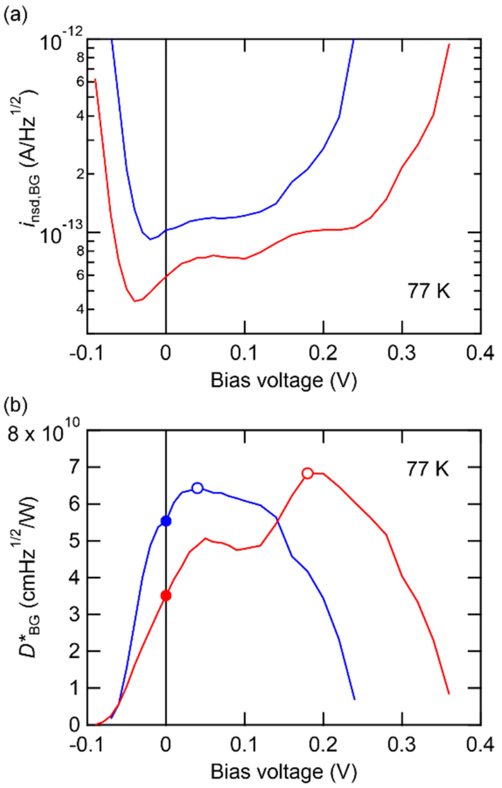

FIG. S6. (a) Bias dependence of current noise spectral density for background state $i_{\text{nsd,BG}}$ at 77 K for QRD (red) and QCD (blue). (b) Bias dependence of the specific detectivity for the background state D^*_{BG} at 77 K for QRD (red) and QCD (blue). Filled circles: zero bias; open circles: peak bias.

of i_{nsd} and D^*, respectively, for the background state. In the flat $i_{\text{nsd,BG}}$ regions in Fig. S6(a) (QRD: -0.01–0.20 V, QCD: 0–0.08 V), the background current overwhelms the dark current. As a result, the detectors operate, in practice, as PV detectors even at $V_b \neq 0$ and can support a great D^*_{BG} value. In fact, as Fig. S6(b) shows, both detectors recorded the maximum D^*_{BG} at finite V_b values within this range. Moreover, this V_b range is wider for a detector with a lower dark current, i.e., with a higher resistance (R_0A). Despite the inferior zero-bias R_{esp}, the QRD offered a higher D^*_{BG} than the QCD at a finite V_b due to its high resistance. By improving the band alignment, the QRD would present much higher D^*_{BG} at a lower finite V_b.

References

[1] F. R. Giorgetta, E. Baumann, M. Graf, Q. Yang, C. Manz, K. Kohler, H. E. Beere, D. A. Ritchie, E. Linfield, A. G. Davies, Y. Fedoryshyn, H. Jackel, M. Fischer, J. Faist, and D. Hofstetter, IEEE J. Quantum Electron. **45**, 1039–1052 (2009).

[2] A. Delga, "Quantum cascade detectors: A review," in *Mid-infrared Optoelectronics*, (Elsevier, 2020), pp. 337–377.

[3] B. F. Levine, J. Appl. Phys. **74**, R1–R81 (1993).

[4] H. Schneider and H. C. Liu, *Quantum Well Infrared Photodetectors: Physics and Applications* (Springer, Berlin, 2007).

[5] C. Koeniguer, G. Dubois, A. Gomez, and V. Berger, Phys. Rev. B **74**, 235325 (2006).

[6] R. Ferreira and G. Bastard, Phys. Rev. B **40**, 1074–1086 (1989).

[7] J. S. Blakemore, J. Appl. Phys. **53**, R123–R181 (1982).

[8] I. Vurgaftman, J. R. Meyer, and L. R. Ram-Mohan, J. Appl. Phys. **89**, 5815–5875 (2001)

[9] C. Jirauschek and T. Kubis, Appl. Phys. Rev. **1**, 011307 (2014).

[10] A. Bigioli, G. Armaroli, A. Vasanelli, D. Gacemi, Y. Todorov, D. Palaferri, L. Li, A. G. Davies, E. H. Linfield, and C. Sirtori, Appl. Phys. Lett. **116**, 161101 (2020).

[11] G. Quinchard, C. Mismer, M. Hakl, J. Pereira, Q. Lin, S. Lepillet, V. Trinité, A. Evirgen, E. Peytavit, J. L. Reverchon, J. F. Lampin, S. Barbieri, and A. Delga, Appl. Phys. Lett. **120**, 091108 (2022).

[12] H. T. Miyazaki, T. Mano, T. Kasaya, H. Osato, K. Watanabe, Y. Sugimoto, T. Kawazu, Y. Arai, A. Shigetou, T. Ochiai, Y. Jimba, and H. Miyazaki, Nat. Commun. **11**, 565 (2020).

[13] M. F. Hainey, Jr., T. Mano, T. Kasaya, Y. Jimba, H. Miyazaki, T. Ochiai, H. Osato, Y. Sugimoto, T. Kawazu, A. Shigetou, and H. T. Miyazaki, Opt. Express **29**, 43598–43611 (2021).